Journal of Materials Chemistry B

ROYAL SOCIETY OF CHEMISTRY

PAPER

View Article Online
View Journal | View Issue

Cite this: *J. Mater. Chem. B*, 2024, **12**, 6654

A plasma-3D print combined *in vitro* platform with implications for reliable materiobiological screening†

Gerardo Hernandez-Moreno, ‡[a] Vineeth M. Vijayan, ‡*[ab] Brian A. Halloran, [d] Namasivayam Ambalavanan, [d] Alexandria L. Hernandez-Nichols, [ef] John P. Bradford,[a] Renjith R. Pillai [a] and Vinoy Thomas *[ac]

Materiobiology is an emerging field focused on the physiochemical properties of biomaterials concerning biological outcomes which includes but is not limited to the biological responses and bioactivity of surface-modified biomaterials. Herein, we report a novel *in vitro* characterization platform for characterizing nanoparticle surface-modified 3D printed PLA scaffolds. We have introduced innovative design parameters that were practical for ubiquitous *in vitro* assays like those utilizing 96 and 24-well plates. Subsequently, gold and silica nanoparticles were deposited using two low-temperature plasma-assisted processes namely plasma electroless reduction (PER) and dusty plasma on 3D scaffolds. Materiobiological testing began with nanoparticle surface modification optimization on 96 well plate design 3D scaffolds. We have employed 3D laser confocal imaging and scanning electron microscopy to study the deposition of nanoparticles. It was found that the formation and distribution of the nanoparticles were time-dependent. *In vitro* assays were performed utilizing an osteosarcoma (MG-63) cell as a model. These cells were grown on both 96 and 24 well plate design 3D scaffolds. Subsequently, we performed different *in vitro* assays such as cell viability, and fluorescence staining of cytoskeletal actin and DNA incorporation. The actin cytoskeleton staining showed more homogeneity in the cell monolayer growing on the gold nanoparticle-modified 3D scaffolds than the control 3D PLA scaffold. Furthermore, the mineralization and protein adsorption experiments conducted on 96 well plate design scaffolds have shown enhanced mineralization and bovine serum albumin adsorption for the gold nanoparticle-modified scaffolds compared to the control scaffolds. Taken together, this study reports the efficacy of this new *in vitro* platform in conducting more reliable and efficient materiobiology studies. It is also worth mentioning that this platform has significant futuristic potential for developing as a high throughput screening platform. Such platforms could have a significant impact on the systematic study of biocompatibility and bioactive mechanisms of nanoparticle-modified 3D-printed scaffolds for tissue engineering. It would also provide unique ways to investigate mechanisms of biological responses and subsequent bioactive mechanisms for implantable biomaterials. Moreover, this platform can derive more consistent and reliable *in vitro* results which can improve the success rate of further *in vivo* experiments.

Received 13th December 2023,
Accepted 17th May 2024

DOI: 10.1039/d3tb02945j

rsc.li/materials-b

[a] *Department of Materials Science and Engineering, Laboratory for Polymers & Healthcare Materials/Devices, The University of Alabama at Birmingham (UAB), 1150 10th Ave S, Birmingham, AL 35233, USA. E-mail: vthomas@uab.edu*
[b] *Laboratory for Polymeric Biomaterials, Department of Biomedical Engineering, Alabama State University (ASU), 915 S Jackson Street, Montgomery, Alabama, 36104, USA. E-mail: vvijayan@alasu.edu*
[c] *Centre for Nanoscale Materials and Bio-integration (CNMB), The University of Alabama at Birmingham (UAB), 1720 2nd Ave S, Birmingham, AL 35294, USA*
[d] *Department of Paediatrics, Division of Neonatology, The University of Alabama at Birmingham (UAB), 1670 University Boulevard, Birmingham, AL 35294, USA*
[e] *Department of Pathology, Heersink School of Medicine, The University of Alabama at Birmingham (UAB), 619 South 19th Street, Birmingham, AL 35233, USA*
[f] *Centre for Free Radical Biology (CfRB), The University of Alabama at Birmingham, 901 19th St S, Birmingham, AL 35294, USA*

† Electronic supplementary information (ESI) available: References to the ESI material will be denoted "Fig. SX". See DOI: https://doi.org/10.1039/d3tb02945j

‡ Equal contribution.

1. Introduction

Nanoparticles have become common in biomedical space with applications in drug delivery, bioimaging, and tissue engineering.[1–7] One of the important challenges associated with the application of nanoparticles is the unreliability of *in vivo* testing as well as the difficulty in scalable and convenient methods for synthesis.[8–10] Specifically concerning nanoparticle surface modifications, application success has largely hinged on the safety and efficacy of *in vivo* testing.[8–10] Most nanoparticles *in vitro* have shown cytotoxicity and the ability to penetrate natural physiological barriers that would normally prevent unwanted and off-target interactions.[11,12] Even with this existing set of challenges, gold and silica nanoparticles have shown great promise in biomedical applications. There is a growing interest in modifying material surfaces like 3D printed scaffolds with nanoparticles for tissue engineering applications such as bone applications.[6,13–15] This strategy for nanoparticle modification changes the surface properties of these scaffold materials to provide favorable cell–material interactions.[10,16] Nanoparticles can be used to modify surfaces either chemically or to modulate certain properties such as surface roughness.[14] Currently, nanoparticle surface modifications are achieved *via* methods including chemical vapor deposition, polydopamine-aided surface coatings and spin coating.[17,18]

This kind of material design control is imperative due to the effect that surface morphology can have on cellular capabilities for surface attachment.[19] Thus, it was evident that nanoparticles play a significant role in the bioactivity of nanoparticle-modified 3D-printed scaffolds.

The scalability of nanoparticle synthesis is a major concern related to the usage of nanoparticles for tissue engineering applications. Most modern large-scale synthesis methods are resource-intensive and/or toxic.[20] Recent biomaterial approaches have made use of low-temperature plasma (LTP) as a scalable method of nanoparticle synthesis.[21–23] The current and environmentally friendly LTP method uses an "alternating current pulse-power driven plasma jet" that creates a reductive environment for more control over the variability of the final product.[24] This LTP process can generate metallic nanoparticles but is confined to aqueous synthesis.[25] Current manufacturing methods have focused on the synthesis of nanoparticles separately from their deposition on target materials like 3D printed scaffolds.[26] As such, nanoparticle applications have focused on particle suspensions or material impregnation rather than surface-anchored nanoparticles.[27,28] Instead of focusing on two independent processes, our group recently developed a novel low-temperature plasma process, namely plasma electroless reduction (PER) to form and deposit gold and silver nanoparticles in one efficient step. Both synthesis and deposition of metallic nanoparticles on polymeric surfaces occur simultaneously using this process.[29] Additionally, our group previously reported another plasma process namely a dusty plasma method for depositing silica nanoparticles on the surface of 3D-printed scaffolds along with other known biomaterials such as PTFE.[30,31] Both these processes, PER and dusty plasma, can modify the surface of 3D-printed scaffold materials with bioactive silica and gold nanoparticles. This clearly suggests the potential of novel plasma-based processes for modifying the surface of 3D printed polymers with nanoparticles.

Traditionally, the interaction of nanoparticles with human cells affecting cellular physiology has been difficult to characterize. This is mainly due to the lack of reliable screening platforms for materiobiological characteristics.[14,32] Materiobiology is an emerging field focused on the physiochemical properties of biomaterials concerning biological outcomes.[33] A biomaterial's physicochemical properties, like surface roughness and compliance, are derived from micro- and nanoscopic features and surface chemistry.[34] These characteristics have been shown to modulate molecular processes in the cell as well as affect the cell structure and migration.[14,19,35,36] Preliminary analysis of new biomaterials, like nanoparticle-modified biomaterials, includes a variety of assays. These include colorimetric viability assays, fluorescence imaging, and gene expression profiling to characterize viability or proliferation. However, the use of biomaterials in these conventional assays does not provide an obvious option for high-throughput screening.[37] The development of a platform that allows for multiple assays to be run in a reliable and reproducible way would have a significant streamlining impact.[37,38] Such platforms with high throughput potential allow for enhanced consistency and reproducibility in studies regarding the biocompatibility and bioactivity of nanoparticle-modified 3D printed scaffold materials.

Inspired by this idea, in the present work we introduce a novel *in vitro* characterization platform with high-throughput capability and future potential. We hypothesized that a combination of reliable and consistent 3D designs with a scalable nanoparticle surface modification process would facilitate more reliable *in vitro* characterization of nanoparticle-modified implantable materials with the capability for more reliable materiobiology screening. Based on this hypothesis, we have combined additive manufacturing and plasma-assisted nanoparticle deposition processes to design a reliable *in vitro* platform to study the materiobiological characteristics of nanoparticle-modified biomaterials. Our main focus was on generating new design parameters for 3D-printed scaffolds with the capability for use in reliable materiobiology screening methods. Secondly, we also employed two low-temperature plasma-assisted *in situ* nanoparticle deposition processes (plasma electroless reduction (PER) and dusty plasma process) to modify our 3D printed designs with silica or gold nanoparticles to demonstrate the modifiability and usefulness of the designs in such biocompatibility studies for 3D printed and surface modified materials.[29,30] To the best of our knowledge, this is the first report that attempts to combine novel 3D printing strategies with plasma-assisted nanoparticle surface modification for developing a reliable materiobiology screening platform. These processes allow the manufacturing of a novel *in vitro* platform for high-throughput biocompatibility testing and characterization of surface-modified materials.[33,39]

2. Experimental section

2.1 Materials

Gold(III) chloride tetrahydrate ($HAuCl_4 \cdot 3H_2O$) (Fisher Scientific, catalogue no G54-5, CAS no 16961-25-4, percent purity- $\geq$49%)

and tetra ethoxy silane (TEOS) (Fisher Scientific, catalogue no AAA14965AE, CAS no 78-10-4, percent purity- 98%) were used as the nanoparticle precursors in this study. 3D printed polylactic acid (PLA) wafers were printed using PLA filaments purchased from FLASHFORGE USA, (Flashforge 1.75 mm PLA 3D Printer Filament, 1 kg Spool) respectively. Harrick Plasma chamber (PDC-001-HP) used for the *in situ* surface reduction process was purchased from Harrick Plasma, New York, USA. Hydrogen gas used for the PER process was purchased from Air Gas company (Ultra High Purity Grade Hydrogen, Size 300 High-Pressure Steel Cylinder, CGA-350).

2.2 Design of the 3D printed PLA Scaffolds

Design requirements were formulated using an iterative approach with development being focused on compatibility with the following cell-cultured treated plates: 96 well plates, 24 well plates, and 12 well plates. The rectangular pore structure was designed to provide a region of interest that would be recognizable and consistent across all samples. SolidWorks was Smaller 3D PLA scaffold wafers, having dimensions of 5.85 mm diameter and 1 mm height, exactly fit inside the well of a 96-well plate and were also designed using SolidWorks. A Flash Forge Creator Max Dual Extruder 3D Printer (Manufacturer-FLASHFORGE USA) was used for all 3D printing processes. 3D printing was achieved using 1.75 mm PLA filaments. The temperature for printing was set to 200 °C and the printing bed was set at 50 °C. A travel speed of 60 mm s^{-1} along with a print speed of 30 mm s^{-1} was used for the printing process and the post-process scaffold was removed from the 3D printer and allowed to cool at room temperature.

2.3 Nanoparticle synthesis and deposition

As reported previously, the gold nanoparticles were generated *in situ* on 3D-printed PLA scaffolds.[29] Briefly, the 96-well plate design 3D wafers were first dipped in 10 mL 250 mM HAuCl4. $3H_2O$ solutions for 5 minutes. Afterward, the dip-coated 3D wafers were placed inside a plasma chamber Harrick Plasma chamber (PDC-001-HP) with the following reaction conditions: 13.56 MHz radiofrequency and plasma power of 45 W. Hydrogen gas at a flow rate of 40 sccm was used to generate plasma inside the chamber for 3 min to facilitate the formation of gold nanoparticles on the surface of the 3D-printed wafers. The PER process was carried out at different time points such as 1, 3 and 5 minutes to optimize the amount of nanoparticle deposition on the surface.

The silica nanoparticles were generated from TEOS using a dusty plasma generation protocol reported previously.[30] Briefly, 300 μL of TEOS liquid was placed inside the Harrick Plasma chamber with the following reaction conditions: 13.56 MHz radiofrequency and plasma power of 45 W, followed by applying a constant air flow rate of 40 sccm inside the chamber *via* an inlet valve. Inside the plasma chamber, adjacent to the TEOS liquid, the 96 well plate design 3D wafers were placed for the *in situ* deposition of silica nanoparticles. The dusty plasma generation process was carried out for different time points such as 1, 3, and 5 minutes to optimize the amount of nanoparticle deposition on the surface.

2.4 Material characterization

The surface features and nanoscale roughness of 3D printed PLA scaffolds modified with gold and silica nanoparticles were systematically studied using a 3D Laser Scanning Confocal Microscope VK-X1000 (developed by Keyence Corporation of America) with nanometre resolution capabilities. Further surface evaluation and surface elemental mapping of the 3D printed scaffold samples was performed using scanning electron microscopy (SEM). Samples were sputter-coated with Au–Pd and observed using an FE-SEM (Quanta FEG 650 from FEI, Hillsboro, OR). Images were taken at different magnifications. The transmission electron microscopy (TEM) imaging of the gold and silica nanoparticles was performed by growing the nanoparticles *in situ* on the copper grid. More specifically, the copper grid was subjected to PER and dusty plasma processes like the 3D-printed scaffolds. After the nanoparticle deposition, these copper grids were imaged using a Tecnai Spirit T12 Transmission Electron Microscope (Thermo-Fisher, formerly FEI) with an operating voltage range of 20 to 120 kV. The X-ray photoelectron spectroscoy (XPS) spectra of silica and gold nanoparticle-modified 3D printed wafers were recorded using a Phi 5000 Versaprobe made by Phi Electronics, Inc. (Chanhassen, WI USA). The instrument's X-ray source is a monochromatic, focused, Al K-alpha source (E = 1486.6 eV) at 25 W with a 100 μm spot size.

2.5 Biological characterization

2.5.1 Cell culture. Validation of the *in vitro* platform was performed using MG-63 (ATCC® CRL-1427™), human fibroblast (Lonza CC-2512), Cos-1 (ATCC CRL 1650), and HBE 16 (ATCC CRL 2741) as the cell models. They were maintained in Eagle's Minimum Essential Medium (MEM 1X) with Earle's salts and without L-glutamine & phenol red (Corning). This was supplemented with 2 mM L-glutamine (Corning), 1X PSF (antibiotic/antimycotic solution, Corning), and 10% fetal calf serum (Hyclone). Cells were passaged using 0.25% Trypsin/2.2 mM EDTA.

2.5.2 Cytocompatibility and cell viability. The wafer 96-well-plate design was used to perform the cell viability MTT (CyQUANT MTT Proliferation Assay Kit, Invitrogen). An ultraviolet 120V SPECTROLINKER® with a UV-C 15-watt 254 nm bulb was used to sterilize the sample surface (6 × 60 seconds, each side) and we were careful to avoid overheating of the PLA samples. 96 well-plate plasma-treated wafers were first placed into the 96 well-plate followed by 30 000 cells per 100 μL complete media being seeded into each well. The plate was put into an incubator at 37 °C with 5% CO_2 for 48 hours. Cell culture media was then replaced with 110 μL of 1 mM MTT solution (negative controls included). A 12 mM stock solution of MTT was made by replacing the cell culture medium with 110 mL of fresh media containing 1 mM MTT including the blank wells and negative controls. The 96-well plates were then set aside to incubate for 4 hours at 37 °C. After incubation, 100 mL of SDS-HCl solution was added to each well and left to incubate for 12 hours overnight at 37 °C. Wafers were removed,

and plates were read using a plate reader set to read at an absorbance wavelength of 570 nm (Bio-Rad).

2.5.3 Fluorescence imaging. MG63 cells were grown on the 96-well-plate design wafer at a cell density of 30 000 cells/100 μL for 48 hours. To characterize cellular proliferation, a Click-iT Plus EdU Alexa Fluor 488 Imaging Kit (Invitrogen) was used along with NucBlue Live Cell Stain ReadyProbes Reagent (Invitrogen). EdU incorporated into newly synthesized DNA in place of thymine was labelled with Alexa-Fluor 488 Azide, while the NucBlue served as the nuclear stain for all nuclei. A green, fluorescent nucleus indicates a proliferating cell, whereas a blue nucleus indicates a nonproliferating cell. ActinGreen 488 ReadyProbes Reagent (Invitrogen) was used to fluorescently stain the cytoskeletal actin in the cell. Approximately 30 000 MG-63 (ATCC® CRL-1427™) cells were plated onto UV sterilized plasma-treated wafers in 96-well plates and incubated at 37 °C and 5% CO_2 for 48 hours. Cells and wafers were incubated with diluted EdU reagent for 4 hours at 37 °C. Cells were then fixed and permeabilized (washed with DPBS, fixed with 4% formaldehyde (Tousimis) for 20 min), washed with DPBS, and permeabilized with 0.25% TritonX-100 (Pierce) for 5 min, and washed with DPBS. The 96 well-plate-designed wafers were then incubated with the diluted Alexa-fluor-488-azide reagent in the Click-It reaction cocktail for 30 min. After washing, fixed cells were incubated with diluted ActinGreen and/or NucBlue reagent for 30 minutes before fluorescent imaging. Samples were imaged using a Nikon Eclipse fluorescent microscope or a Nikon A1R HD Confocal Microscope. The software used was NIS Elements 5.0 Imaging Software for post-processing.

2.5.4 Alizarin red biomineralization. MG-63 (ATCC® CRL-1427™) cells were grown on 96-well-plate PLA scaffolds with or without gold nanoparticle modification for 21 days. Alizarin Red staining was performed on day 21. Briefly, cells were washed with PBS and then fixed in 4% PFA in PBS. Cells were then washed with PBS and stained with a 2% solution of Alizarin Red (Sigma CAS 130-22-3 Product No. A5533) in high-purity water at pH 4.2–4.5 for 45 min at 25 °C protected from light. Cells were then washed with high-purity water and semi-quantitative colorimetric images were acquired on a GE Healthcare Amersham 600 Series Imager. Image analysis was performed with the ImageJ ReadPlate 3.0 Plugin.

2.5.5 Alkaline phosphatase assay. The alkaline phosphatase (ALP) activity assay was performed using the 96-well-plate wafer design, using the 1-Step PNPP assay (*p*-nitrophenyl phosphate disodium salt) (Pierce). The 96-well-plate wafers were first placed into the 96-well-plate followed by 30 000 cells per 100 μL complete media being seeded into each well. The plate was then set aside to incubate at 37 °C with 5% CO_2 for 48 hours. The 1-Step PNPP solution was added, 100 μL to each well. The plate was then incubated for 30 minutes at which point the colour developed. We then added 50 μL of 2 N NaOH to stop the reaction and mixed the solution *via* agitation. The absorbance was read using a plate reader with the absorbance set to 405 nm (Bio-Rad).

2.5.6 BioTEM Imaging. MG-63 (ATCC® CRL-1427™) cells were grown on both gold plasma treated and control Costar® Transwell® 6.5 mm diameter inserts with a 0.4 μm pore size tissue treated polyester membrane (Corning). The cells were plated at 30 000 cells per 400 μL of complete media into a 24-well plate. The plate was set to incubate for 48 hours at 37 °C and 5% CO_2. After incubation, the cells were fixed using 3% glutaraldehyde in 0.1 M cacodylate buffer for 60 minutes. The plates were left to incubate at 4 °C overnight. The cells were then fixed once again in 1% OsO_4 for 45 minutes. The cells were then dehydrated using ethanol using a series of dilutions up to 200 proof. Using Epon-812 epoxy resin the cells on the inserts were infiltrated and embedded. After curing, thin sections were cut using a diamond knife with a Leica UC6 ultramicrotome. These sections were counterstained with uranyl acetate and lead citrate for further contrast. TEM images were taken using an FEI Tecnai Spirit electron microscope and AMT digital camera.

2.5.7 Ponceau S total protein staining. Ponceau S protein staining was performed on untreated PLA or gold nanoparticle-treated scaffolds that had been incubated with 5× diluted human plasma for 48 h at 37 °C. Briefly, Ponceau S solution (Sigma on the scaffolds then scaffolds were subsequently washed 3× with ultrapure water). Colorimetric images were obtained *via* GE Healthcare Imager.

2.5.8 Fluorescein conjugated BSA protein absorption assay. 200 μg of fluorescein conjugated BSA was incubated with untreated PLA or gold nanoparticle-treated scaffolds for 1 h at 37 °C. Then the scaffolds were washed 3× with PBS. Fluorescence was then measured at 488ex/520em using a BioTek plate reader. Data were quantified using a standard curve.

2.5.9 Proteinase K digestion. Untreated PLA or gold nanoparticle-treated scaffolds were incubated with human plasma for 48 hours. The scaffolds were then washed with PBS and incubated with 50 μg mL^{-1} proteinase K at 37 °C for 1 h. The reaction was stopped by the addition of 2 mM EGTA (pH 8.0). The samples were centrifuged at 10 000 × *g* for 10 min at 4 °C. A DC Lowry protein assay was performed for protein quantification.

2.6 Statistical analysis

GraphPad's Prism software was used to perform all statistical analyses throughout this study. More specifically, the MTT assay data (Fig. 5(a)) were analysed using one-way ANOVA analysis of variance, with degrees of freedom (d*F*n) between columns of 9, degrees of freedom within columns (d*F*d) of 40, total degrees of freedom, and an *F* value of 29.03 [*F* (d*F*n, d*F*d) = 29.03].

3. Results and discussion

A major advancement in tissue engineering is the use of 3D printing materials which has advanced the field and opened doors to *in vitro* testing of new biomaterials; however, the methodology is often overlooked when characterizing these materials.[40] To perform *in vitro* testing using 3D-printed biomaterials, groups often need to cut or manipulate their material or print very small constructs to be used in larger well plates to allow for the proximity of the material to the cell

monolayer.[41–43] Most commonly, groups produce extracts of the material being tested and then expose cell cultures to these materials at pre-determined concentrations as a liquid or pharmaceutical treatment.[41] Other groups grow their cell model on their respective materials and are then required to detach the cells for analysis in separate dishes or well plates.[42] This can be an issue related to time and material waste concerning critical cell-based assays for analysis of biocompatibility. Recent advances in 3D printing for biomaterials have led to the 3D bioprinting method; however, the value of traditional 3D printing with simple polymers such as PLA should not be ignored given the ability to modify the surfaces of these materials.[44] In the present work, we have combined novel 3D scaffold designs and a plasma-assisted nano structuring process to engineer a materiobiology platform which can be used to study the materiobiology characteristics of gold and silver nanoparticle modified 3D printed PLA scaffolds.

3.1 Engineering new design parameters for 3D-printed scaffolds with the capability for conducting reliable materiobiology studies

Initially, we formulated new design parameters to fit the needs of both material characterization methods as well as common *in vitro* assay labware. Designs were centered around the most commonly used cell culture vessels including 96, 24 and 12 well plates. The ideation phase yielded the following engineering requirements: (1) ease of handling, (2) materiobiological screening, (3) ease of 3D printing, (4) expandable in size, (5) built-in scale, and (6) open-source friendly (easy to redesign and modify). Three main designs were successfully printed with effective size and scale maintained despite the high resolution required for the 96-well-plate wafer (Fig. 2(a)–(c)).

We have purported a method for utilizing new designs in 3D printing scaffolds that could allow for high-throughput assessment of nanoparticle-modified materials. Design parameters for these 3D-printed scaffolds were set practically for ubiquitous *in vitro* assays such as those utilizing 96, 12 and 24-well plates. The pores' 1 mm × 1 mm design gave access for most tweezers to grab and remove the wafers without damaging any cells attached for sensitive tasks such as fluorescent imaging. The pore dimensions served as a scale during microscopy and imaging which simultaneously served as a consistent region of interest thus ensuring reproducibility and reliability (Fig. 2(c)). Finally, in the designing of this method, we accounted for the practicality of the technique; hence, the design is easy to modify with minimal training in CAD software and can be printed in large quantities in one print, translating to better scalability depending on future needs and applications (Fig. 1). More reliable materiobiological characteristics of nanoparticle-modified biomaterials, such as their physicochemical properties, biocompatibility studies, and bioactivity studies can be determined using these new designs. This would improve the reliability of *in vitro* results which can improve the *in vivo* and preclinical success of nanoparticle modified biomaterials.

We selected a 96-well-plate wafer as the base design, which was engineered with a 3 × 3 grid of square pores with dimensions of

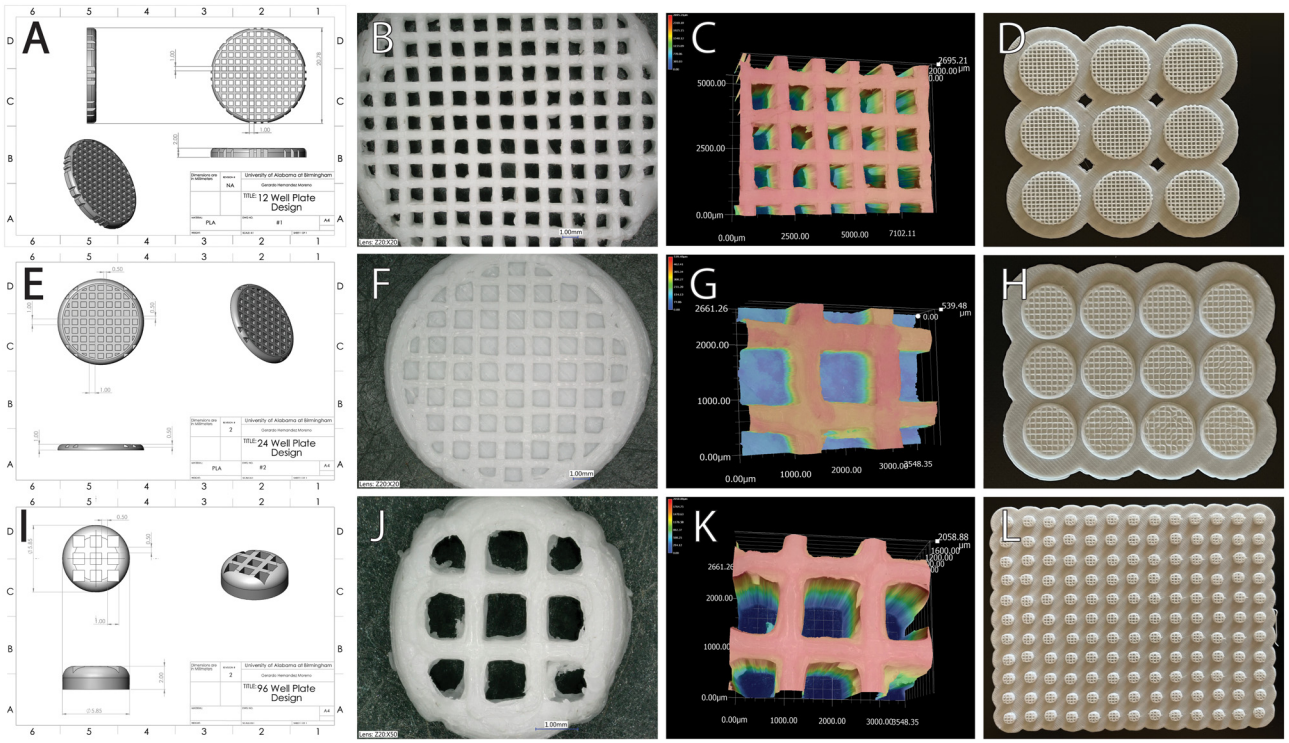

Fig. 1 Wafer designs. All wafers were designed using Solid Works CAD software. (a), (e), and (i) Wafer part drawings from the 12-well-plate, 24-well-plate, and 96-well-plate, respectively. (b), (f), and (j) Top view of the 12-well-plate, 24-well-plate, and 96-well-plate wafers respectively; (c), (g), and (k) Keyence analysis of the wafers in the 12-well-plate, 24-well-plate, and 96-well-plate respectively, confirming final print measurements consistent with CAD drawings; (d), (h), and (l) Top view images of the final wafer prints from the 12-well-plate, 24-well-plate, and 96-well-plate, respectively.

1 mm side lengths, resulting in a central pore that acts as a region of interest (ROI) that remains objectively consistent from sample to sample (Fig. 1(c)). This format was utilized heavily in our studies as it is the most commonly used format for cell-based assays. The design also gives the ability to print various samples at one time thus increasing sample consistency and decreasing batch-to-batch variation stemming from manual sample preparation (Fig. 1(c)). Confocal laser scanning microscopy imaging showed that the printed wafers were consistent with the dimensions of the CAD models and would ultimately retain their function (Fig. S1–S3, ESI†). The dimensions from these scans were calculated *via* Keyence imaging software and have been tabulated (Fig. S6, ESI†).

3.2 Application of low temperature plasma on the new 3D designs and reliable investigation of the material properties

The Plasma Electroless Reduction (PER) and dusty plasma processes developed by our group were used to modify the 96 well-plate-sized wafers *in situ*.[29,30] More specifically in the PER process, the process chemistry behind the formation of gold nanoparticles was the surface reduction of the gold salts from a higher oxidation state to lower one using hydrogen plasma as a reducing agent. This process was found to uniformly and stably attach gold nanoparticles on 3D printed PLA surfaces.[27] In the case of dusty plasma assisted formation of silica nanoparticles, the process chemistry was the plasma polymerization of the reactive tetraethoxysilane monomer which, when using a small volume (300 μl) and exposure time (5 minutes), polymerizes and deposits uniform and stable silica nanoparticles on the surface of 3D printed PLA. We believe that a combination of the new 3D printed PLA designs and the 2-nanoparticle forming plasma process can form a reliable platform for evaluating the materiobiology of gold and silica nanoparticle modified polymer surfaces.

The initial aim was to optimize the deposition of both gold and silica nanoparticles on 3D-printed 96-well plate design scaffolds. This was accomplished by varying the time course of exposure of both PER and the dusty plasma process using the following time points: 1 min, 3 min, and 5 min (Fig. S4, ESI†). These time points were tested due to the results in a previous study synthesizing silver nanoparticles.[29]

First, to observe differences in nanoparticle synthesis and formation, a transmission electron microscope (TEM) grid was modified using dusty plasma and the PER processes. The TEM grid was subjected to the dusty plasma process to form silica nanoparticles or to the PER process to form gold nanoparticles on the surface. After the nanoparticle deposition, the modified copper grids were imaged using TEM and showed a varied sizing distribution throughout the grid for both treatments (Fig. 2(a) and (b)).

The gold nanoparticle-treated grids contained both smaller-sized gold nanoparticles (~20 nm) and larger gold nanoparticles (~100 nm) (Fig. 2(a)). The observed formation of both smaller and larger gold nanoparticles may be attributed to a nucleation process where initially smaller gold nanoparticles form and subsequently many of them grow into larger gold nanoparticle clusters (Fig. 2(a)). The important observation was that the distribution of these gold nanoparticles was highly uniform and consistent across the entire TEM grid. This clearly shows that the gold nanoparticle formation *via* the PER process is very uniform and homogenous. In the case of silica-treated samples, the nanoparticles formed as beads or grape-like clusters of silica nanoparticles with particle size ~200 nm (Fig. 2(b)). The deposition of silica on the TEM grid showed partial coverage with a lot of empty spaces in the grid.

Scanning electron microscopy (SEM) was used to confirm the nanoparticle synthesis and deposition (Fig. 2(c)). This confirmed the presence of silica and gold nanoparticles on the surface of the 3D-printed wafers. We also employed the use of X-ray photoelectron spectroscopy (XPS) to confirm these results (Fig. S5, ESI†). Notably, the differences in nanoparticle deposition between the silica and gold are visible *via* SEM (Fig. 2(c)). The silica nanoparticles, synthesized and deposited using the dusty plasma method, aggregated to a greater extent than the gold samples. The gold nanoparticles' deposition was more homogenous on the treated surface. An energy-dispersive X-ray spectroscopy (EDAX) system was used to study the distribution of gold and silica nanoparticles formed on the surface of the 3D PLA wafers. XPS and EDAX analyses were then utilized primarily to demonstrate the presence of gold and silica on the modified materials (Fig. 2(d)). The results showed non-homogenous distribution of silica and oxygen atoms on the surface of 3D PLA scaffolds modified by silica nanoparticles whereas the gold nanoparticle surface mapping clearly showed a homogenous and uniform distribution of gold throughout the surface of 3D PLA scaffolds (Fig. 2(d)). The confocal laser surface scanning microscopy method was used to corroborate the distribution of gold and silica nanoparticles formed on the surface of the 3D PLA wafers that were previously assessed *via* EDAX (Fig. S5a–c, ESI†). Images showed silica nanoparticles followed a time-dependent deposition, evident due to the increased nanostructuring occurring on the surface of the wafers (Fig. S5a, ESI†). The unique 96-well plate-sized 3D PLA design made it efficient to compare the formation of both gold and silica nanoparticle formation over the surface. This design allows for the performance of more reliable and consistent comparisons from sample to sample regardless of the surface treatment used.

These results demonstrate clear differences between the dusty plasma and PER treatments. The gold nanoparticle modification was uniformly distributed over the surface, unlike the silica nanoparticles. The silica nanoparticles were formed as clusters and did not cover the entire surface. The SEM and TEM data corroborated previous data regarding the formation of gold and silica nanoparticles on the surface of 3D PLA scaffolds (Fig. 2). The results of different morphological characterizations such as SEM, EDAX surface mapping, and TEM imaging support this observation.

Gold nanoparticles resulting from the plasma electroless reduction method appear uniformly and stably anchored on the 3D printed surface. However, silica nanoparticles made using the dusty plasma process were inconsistent and less particle stability was observed. Dusty plasma makes use of plasma polymerization for its mechanism, a chaotic and random process. This most likely

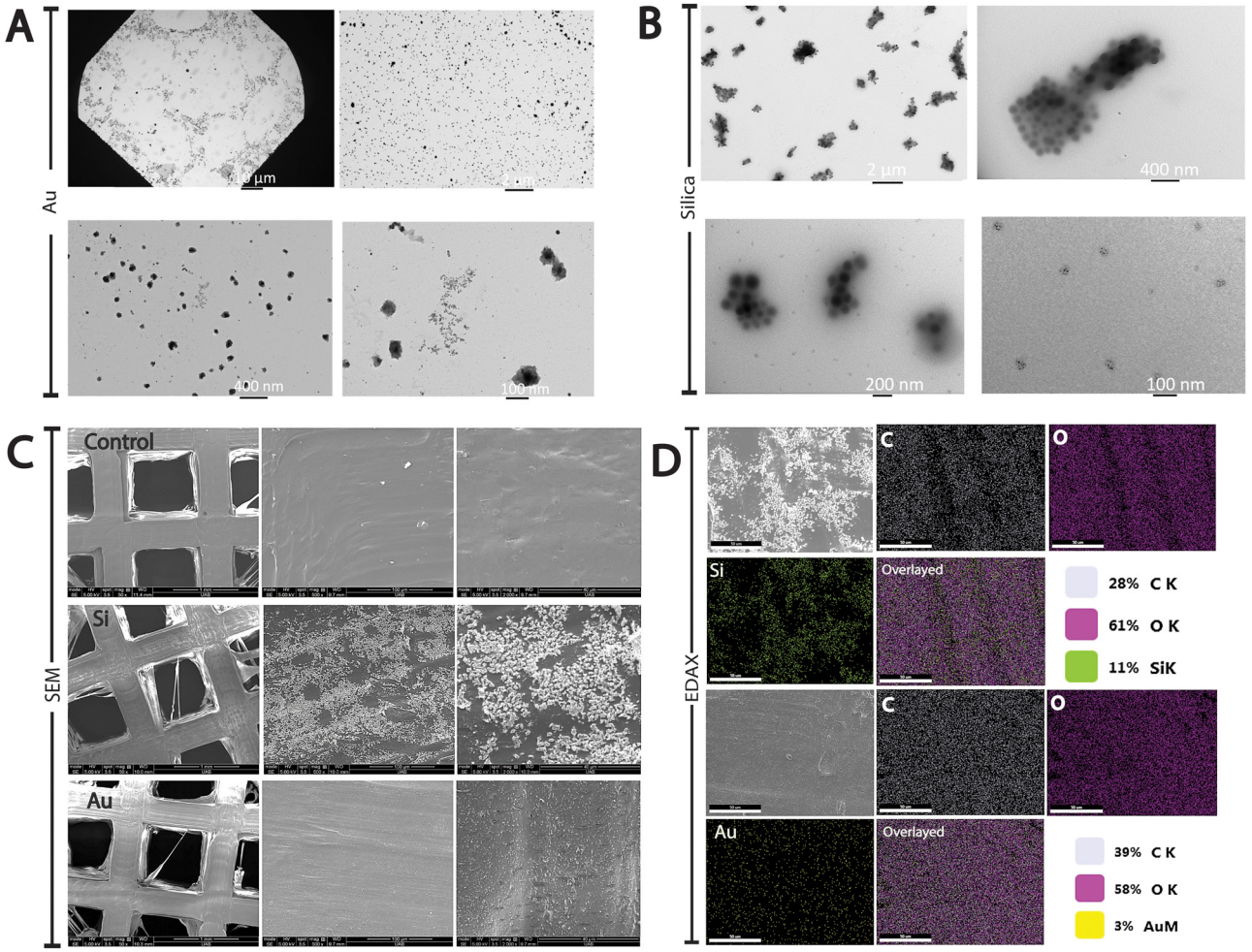

Fig. 2 Nanoparticle deposition confirmation using TEM and SEM imaging. (a) and (b) Confirmation of the particle size of gold and silica nanoparticles using TEM imaging of nanoparticle-modified copper grids. TEM shows the differences between the deposition occurring from the plasma electroless reduction (PER) process *versus* the dusty plasma process. The deposition of gold nanoparticles is uniform, and the presence of nanoparticles is observed. (c) Confirmation of nanoparticle deposition on 3D printed PLA scaffolds using SEM imaging. (d) EDAX mapping images of gold and silica nanoparticle modified 3D PLA scaffolds confirming nanoparticle composition and placement.

contributes to the inconsistent deposition of silica nanoparticles. Whereas, with the plasma electroless reduction (PER) process, gold nanoparticles are formed *in situ* on the surface of the 3D PLA scaffolds. Also, the post-sonication wash step ensures that only stable and uniformly anchored gold nanoparticles remain on the surface.[29] This difference in the nanoparticle modification process on the 3D PLA surface was visible in the biological responses of these nanoparticle-modified scaffolds. Low-magnification images were taken of the surface to observe general attachment and the presence of cellular attachment on the surface. More specifically, the actin fluorescent images demonstrated the homogeneity of the cellular attachment which correlated to the distribution of nanoparticles on the surface of the scaffolds.

3.3 Reliable investigation of biological responses using the combined platform of 3D printing and plasma

To establish the compatibility of the nanoparticle-coated PLA substrates with cell growth, several *in vitro* assays utilizing an osteosarcoma pre-osteoblast cell line, MG-63 (ATCC® CRL-1427™) were performed. The MG-63 cell line was utilized for these initial studies due to the relevance of both silica and gold nanoparticles in osteo-engineering and biocompatibility.[16,45–48] The 96-well plate design was used for viability assessments with the CyQUANT MTT Cell Viability Assay (Invitrogen). The 96-well-plate PLA wafers were used to assess MG-63 cell viability and growth on the wafers (Fig. 3). Two sets of controls were used to compare each nanoparticle treatment group: a set of "plated cells" that contained no PLA substrate or nanoparticle treatment; and a PLA wafer with no low-temperature plasma treatment. Due to the PLA not containing any other blended materials or additives, no significant impact on the biocompatibility of the material was expected, since PLA has been previously explored and used effectively in biomedical applications.[36]

Fluorescent actin staining (ActinGreen 488 Ready Probes Reagent, Invitrogen) was used to visualize the cytoskeleton of the cells. Non-treated PLA-control wafers showed portions with significant confluency but had areas on the surface and in the pores that showed inhibited growth and overall cell attachment

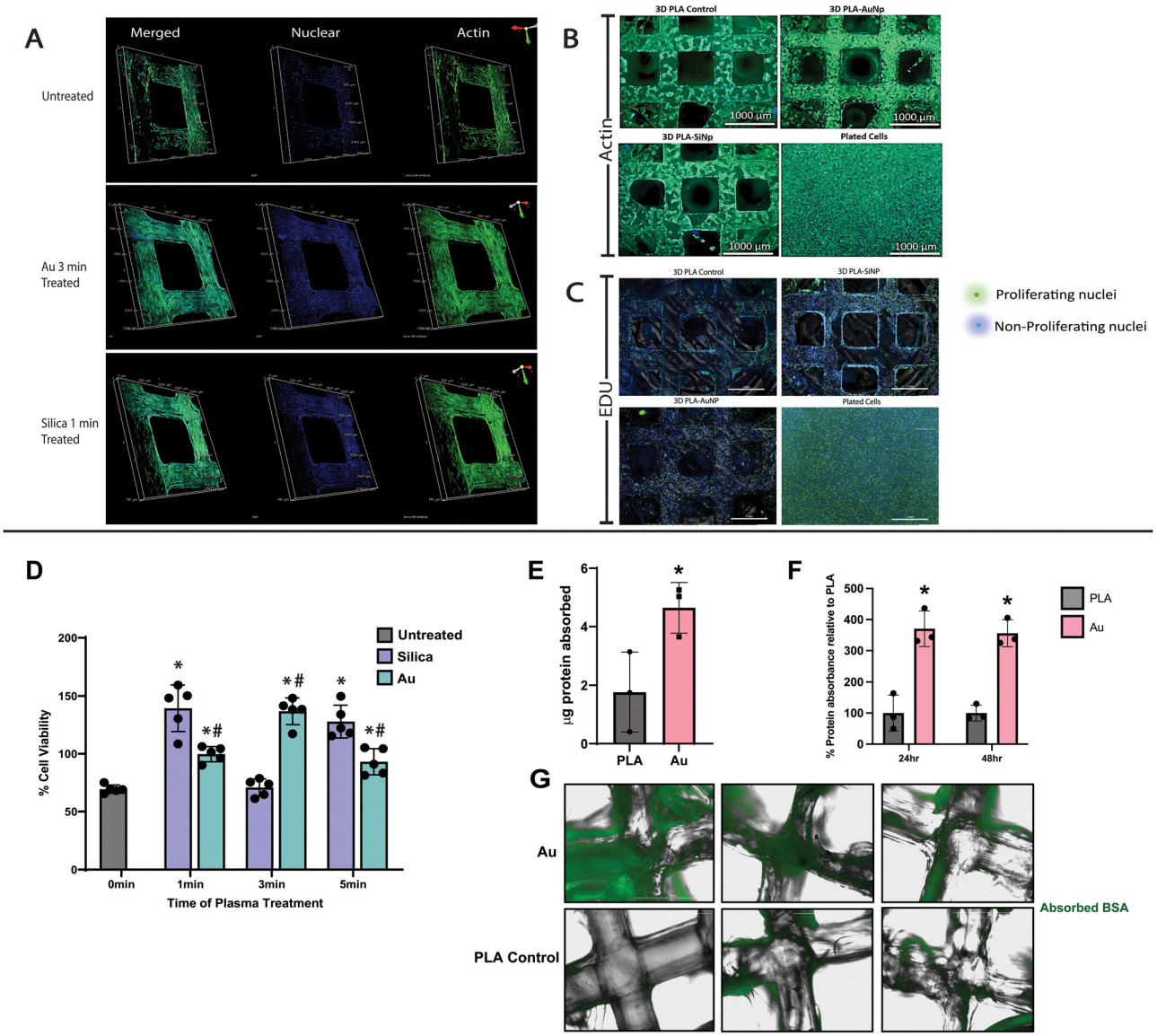

Fig. 3 Gold nanoparticle modification *via* the LTP-process increases cell attachment and protein adsorption compared to non-modified 3D-printed wafers. (a) Confocal fluorescence images of the gold and silica nanoparticle-modified 3D-printed PLA scaffolds. Images show actin fluorescence staining of both the gold and silica nanoparticle-modified 3D-printed PLA scaffolds. Images were taken using a Nikon A1R HD Confocal Microscope. Cells were plated at 30 000 cells per well and incubated for 48 h. (b) Fluorescent actin staining images of MG-63 cells grown on a 96-well-plate wafer. Imaged using a Nikon Eclipse fluorescent microscope. Cells were plated at 30 000 cells per well and incubated for 48 h. (c) EdU cell proliferation images of MG-63 cells grown on a 96-well-plate wafer modified with gold and silica nanoparticles. Cells were plated at 30 000 cells per well and incubated for 48 h. (d) MTT cell viability assay performed on MG63 cells grown on gold or silica nanoparticle modified 3D PLA scaffolds for 48 hours. Analysed using one-way ANOVA. *$p < 0.05$ compared to untreated; #$p < 0.05$ compared to silica (n = 1 independent experiment with 5 replicates). (e) Fluorescein labelled BSA was incubated with PLA control scaffolds and gold nanoparticle-modified scaffolds for 1 hr at 37 °C. Samples were washed and then fluorescence was measured. * = $p < 0.05$ compared to PLA. (f) Representative images of gold nanoparticle-modified and PLA control scaffolds incubated with BSA-Fluorescein. (g) Healthy human donor plasma was incubated with PLA control scaffolds and gold nanoparticle-modified scaffolds for 24 or 48 h at 37 °C. Samples were washed and then stained. * = $p < 0.05$ compared to PLA.

(Fig. 3(a) and (b)). The samples treated with dusty plasma showed similar cell attachment to that of the control untreated wafer. Cells were confluent in some parts of the surface, but not others. This was consistent with the previously observed uneven distribution of particles on the surface. However, the gold nanoparticle-treated wafers had consistent cell growth across the surface (Fig. 3(a) and (b)). These results support the previous trend of even gold nanoparticle deposition using the PER process (Fig. 2).

Cell proliferation on nanoparticle-coated wafers was assayed with Click-iT Plus EdU Alexa Fluor 488 Imaging Kit (Invitrogen), which detects active cell proliferation. The MG-63 cell EdU stained nuclei fluorescent images showed the same cell growth pattern seen in the previous images using the actin dye

(Fig. 3(c)). The control wafer sample had a lack of uniform growth. The uniformity of the cell growth on the silica wafers varied greatly between samples because of the high variability observed in the dusty plasma method. No major differences in cell proliferation between the different groups were observed.

After forming the nanoparticle-modified scaffolds, we tested the effects on cytotoxicity.

The cytocompatibility was tested using an MTT assay, which assesses cellular metabolic activity and reflects cell viability (Fig. 3(d)). The cells plated on a tissue culture plate without a PLA wafer were used as a positive viability reference. The experimental design included similar groups to that of the Keyence confocal laser scanning microscopy analysis (Fig. S5, ESI†). The 1- and 3-min gold nanoparticle-treated samples showed a significant increase in viability compared to the untreated control PLA wafers. However, the 3 min PER treated PLA wafers maintained higher cell viability compared to the 1 min PER and untreated PLA wafers. The silica-treated PLA wafers showed no significant difference in viability between groups.

Gold nanoparticle sample variability remained consistent while the silica group varied depending on the length of treatment (Fig. 3(d)). The plasma treatments introduced variability in the silica coating. This is a limitation of the plasma method (Fig. 3(d)). A post-processing washing step was previously introduced and increased cellular viability by removing unstable and non-anchored particles that were toxic.[29] Both gold and silica nanoparticles would be cytotoxic without this wash step.[29] The cell viability data demonstrated there were significant changes in the viability of Au and Silica treatments to no treatment at all. Au and silica were also significantly different from each other with Au showing the best viability (Fig. 3).

Given these results, we aimed to test a potential mechanism for how gold nanoparticles were preventing cytotoxicity and discontinued further cell biocompatibility analyses with the silica nanoparticles. We hypothesized that the gold nanoparticles provide anchoring points for cells and are achieving this by adsorbing cellular proteins on the scaffolds' surface. We used an *in situ* fluorescein-conjugated BSA protein assay whereby we measured the adsorption capacity of the 3D-printed gold-treated test wafers. Gold nanoparticle-modified scaffolds showed a doubling of protein adsorption compared to un-modified PLA scaffolds (Fig. 3(e) and (g)). Consequently, we decided to test if this effect occurs with physiologically relevant proteins. We then performed *ex vivo* human sample studies comparing gold-treated samples to untreated PLA control wafers. We found that significant protein adsorption occurred in the gold nanoparticle-modified scaffolds incubated for 48 h compared to the PBS controls (Fig. 3(f)). This is a notable observation due to previous work done by others showing that gold nanoparticles coated in albumin protein have demonstrated increased biocompatibility and bioavailability.[49]

3.4 Surface characterization of gold nanoparticle-treated wafers incubated in simulated body fluid

The gold-treated wafers were incubated in simulated body fluid and showed significant differences between the gold-treated and untreated wafers (Fig. 4). Surface characterization, of both the untreated and gold nanoparticle-modified wafers, was performed using SEM, energy dispersive X-ray microscopy (EDAX), and X-ray photoelectron spectroscopy (XPS) (Fig. 4 and 5). The representative images taken *via* SEM (Fig. 4) showed an

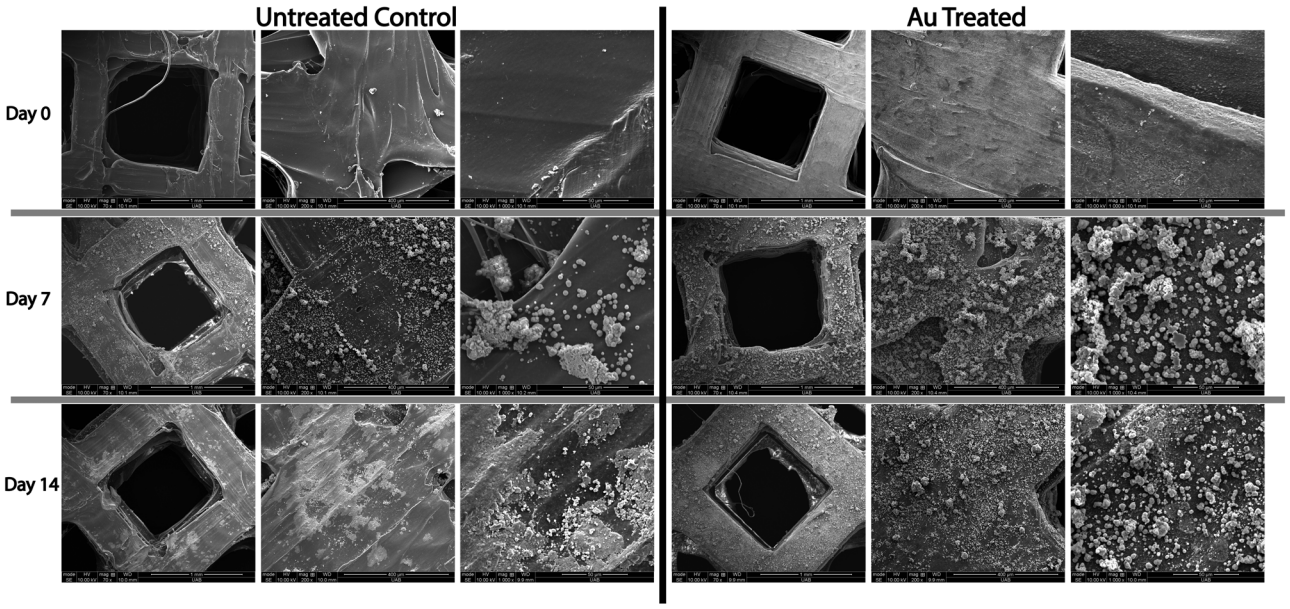

Fig. 4 Mineralization occurring after incubation in a simulated physiological environment confirmed using SEM imaging. Control and gold nanoparticle-treated wafers were left to incubate in simulated body fluid (SBF) for a total period of 14 days. Scanning electron microscopy revealed microstructuring occurring after a minimum incubation period of 7 days. Samples imaged at 14 days appear to have increased particle deposition. Gold nanoparticle-treated wafers resulted in increased mineralization deposition compared to the untreated wafer controls. (Each column of images was taken at the same magnification and other settings for consistent and reliable comparison.)

increased deposition of microstructures on the surface of both the untreated PLA wafers and the gold nanoparticle-modified PLA wafers. However, the gold nanoparticle-modified PLA wafers resulted in a higher presence of nano/microstructures on the surface when compared to the unmodified PLA control wafers. Moreover, the deposition occurring at about 7 days of incubation appears to plateau in simulated body fluid (SBF). Subsequently, EDAX was then used to confirm the presence of calcium, most likely in the form of calcium phosphates given the presence of phosphorous present in the XPS data as previously reported by our group.[50] XPS was used to confirm the mineralization occurring on the surface of the gold nanoparticle-modified wafers as seen in the SEM images (Fig. 5). XPS data then confirmed the presence of mineral

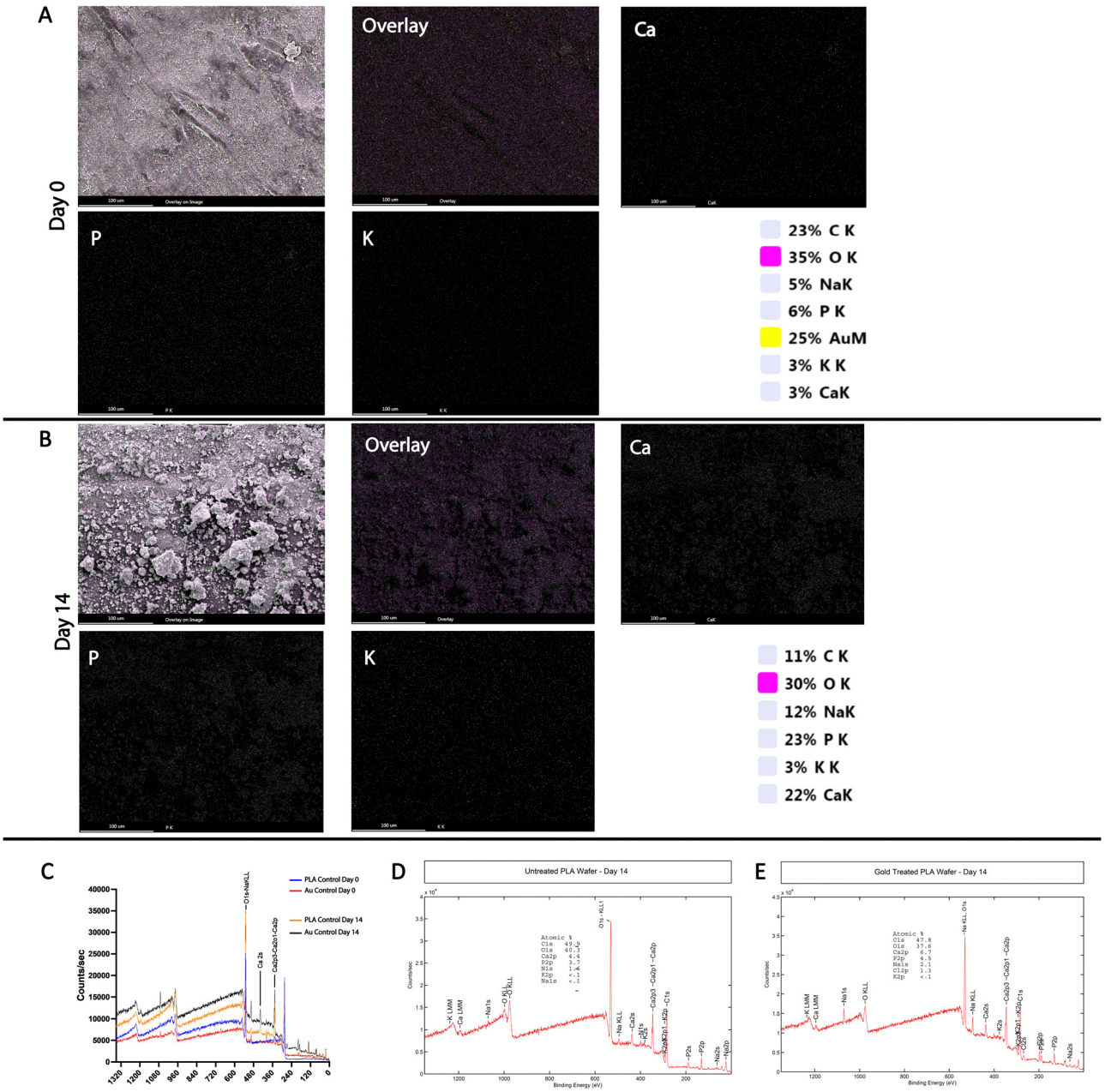

Fig. 5 Using EDAX and XPS confirmation of calcium-based mineralization deposition onto the surface of gold-treated 3D-printed wafers. (a) and (b) Images were taken using SEM and EDAX to confirm the presence of mineralization-related elements. The main elements of interest consisted of Ca, P, Na, and K. The images from panel A compare a gold-treated wafer that has not been exposed to simulated body fluid to one (panel B) that has been incubating in simulated body fluid for 14 days. The 14-day sample images demonstrate an increased amount of mineralization consisting mostly of Ca, P, and K. (c) Combined graphs of XPS graphs for untreated PLA controls and gold-treated PLA wafers that were incubated in simulated body fluid (SBF) for 14 days. A set of non-incubated samples are compared to a set of 14-day incubated samples. Graphs are overlayed to achieve a closer comparison. (d) and (e) Individual XPS graphs were generated using the instrument's software denoting the resulting elemental analysis. Individual graphs are shown along with the composition analysis. More information concerning the control samples tested can be found in Fig. S6 in the ESI.†

deposition on the surface of the wafers along with the presence of calcium and phosphorous, most likely due to the resulting calcified mineralization seen in the SEM imaging (Fig. 5(c)).

The resulting images *via* SEM showed a significant increase in the mineralization-related spherical growth on the surface of the wafers (Fig. 4). This was also verified and corroborated using XPS and EDAX (Fig. 5). The literature suggests that spherical growth observed in the treated samples may indicate the presence of hydroxyapatite spherical particles.[51] Our findings suggest that gold nanoparticle-treated PLA encourages the growth of hydroxyapatite formation on the surface of a given substrate. They also suggest that the hydroxyapatite particles grown are likely to be spherical and thus encourage positive biocompatibility in osteogenic relevant environments.[51]

3.5 Elucidating a potential mechanism of action for cellular attachment using biological TEM

To gain more insight into the mechanistic insights of better cytoskeletal spreading of MG-63 cells on the gold nanoparticle-modified surface, we used biological TEM to image the cross-section of MG63 cells growing on a gold nanoparticle treated *trans* well membrane (6.5 mm, 0.4 μm pore, Costar) (Fig. 6). Cellular interaction with the substrate surface was characterized and demonstrated very limited particle absorption (Fig. 6). The interface between the cell and the membrane contained synthesized gold nanoparticles that are visible and are absent in the control images (Fig. 6). Furthermore, the cellular behaviour showed the cytoskeleton generating projections and extending toward the gold nanoparticles in the gold treatment group. Most notably, biological TEM suggested that the gold nanoparticles may serve a role in cytoskeletal interaction or structure. These important images did not show any signs of phagocytosis of the nanoparticles that, based on the literature, would most likely cause cytotoxic effects through DNA corruption or other mechanisms.[8,9,27,52]

Furthermore, functional effects were analysed using the MG-63 cell model and by performing mineralization assessments using an Alizarin Red Dye Cellular Staining Assay (Sigma) and Alkaline Phosphatase Cellular Activity Assay (ALP) (Thermo) (Fig. 7(a) and (b)). To establish the compatibility of the gold-nanoparticle-coated PLA substrates with cell growth, several *in vitro* assays were utilized. The 96-well-plate design was used for viability assessments. A CyQUANT MTT Cell Viability Assay (Invitrogen) was performed for 3 cell lines (human Fibroblasts, Cos1, and HBE16) (Fig. 7(c)).

Mineralization assessments were performed using both Alizarin Red staining (an assay for the presence of free calcium) and ALP activity assays (a measurement of alkaline phosphatase activity) in MG-63 cells to demonstrate the ability of this platform to allow for cellular staining as well as enzymatic activity. The cells plated on a tissue culture plate without PLA scaffolds, were used as a positive viability reference. Fig. 7(a) shows results from the enzymatic ALP assay which elucidated changes in ALP activity over 3 weeks in cells from the untreated PLA control and gold nanoparticle-treated group compared to the controls. Fig. 7(b) shows the free calcium, assessed with Alizarin Red staining, increased equally in un-modified PLA or gold nanoparticle-modified PLA groups over 3 weeks. The cytocompatibility was tested using an MTT assay, which assesses cellular metabolic activity and reflects cell viability (Fig. 7(c)). Gold nanoparticle-modified samples showed a significant increase in viability compared to the un-modified control PLA scaffolds in all three

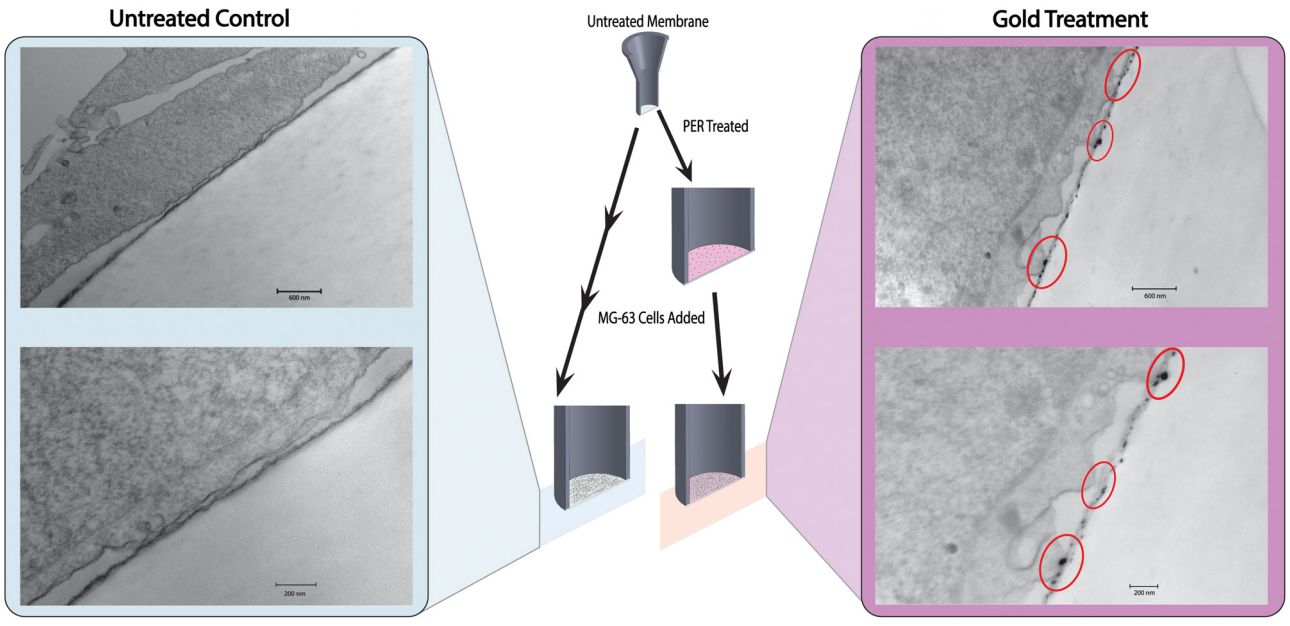

Fig. 6 Cytocompatibility validation using biological TEM. MG-63 cells were grown on Transwell membrane well inserts. Cross-sectional images were taken using biological TEM showing the interface between the treated or untreated membrane to elucidate a potential mechanism of action for cell attachment and to determine if there was any incorporation of nanoparticles in the cell. (a) Untreated control cell and membrane image. (b) PER treated Transwell membrane. Images were taken using the FEI Tecnai Spirit electron microscope and AMT digital camera.

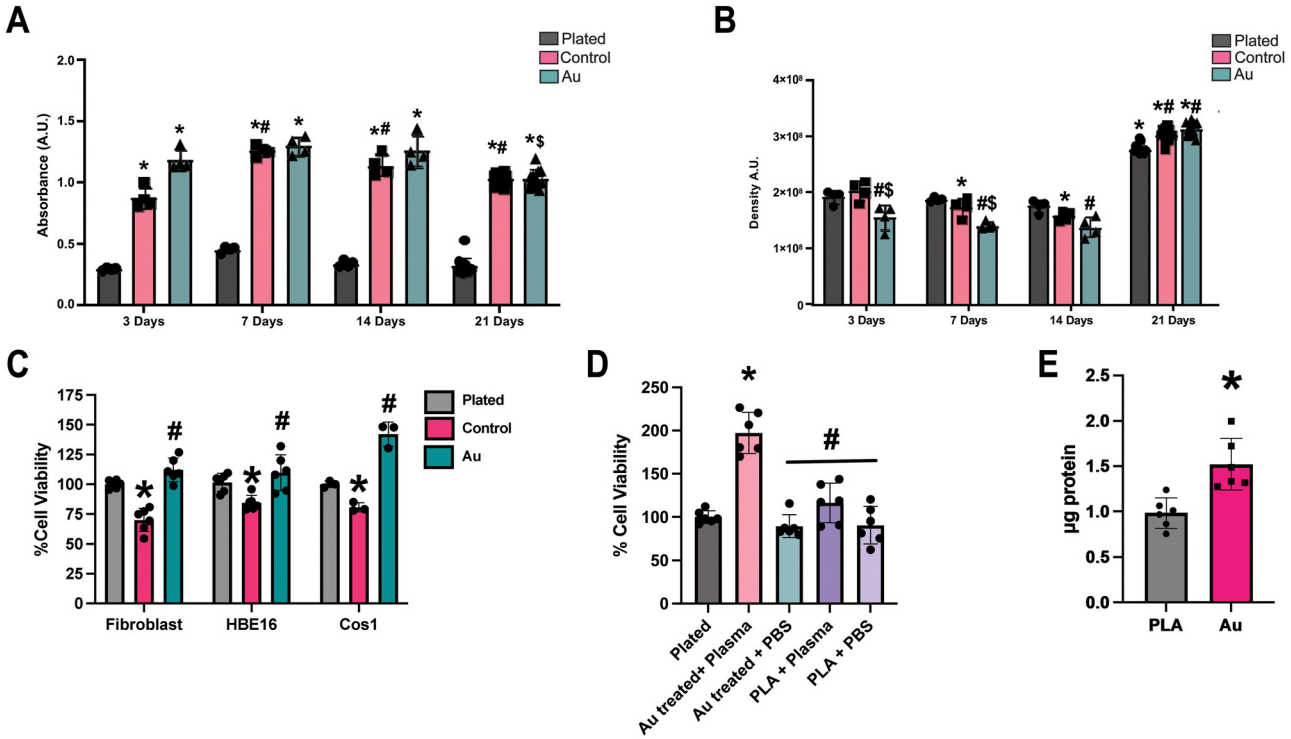

Fig. 7 Use of 3D-printed scaffolds, modified with gold nanoparticles, increases viability and functional processing of multiple cell models, and incubation in human plasma increases cell viability and general protein adsorption. (a) An alkaline phosphate assay (ALP) was performed on MG-63 cells grown on gold nanoparticle-modified PLA or unmodified PLA scaffolds for 3, 7, 14, or 21 days. Analysed using two-way ANOVA. *$p < 0.05$ compared to plated; #$p < 0.05$ compared to control day 3; \$$p < 0.05$ compared to gold day 3. Data are $n = 5 \pm$ SD. (b) Alizarin Red staining was performed on MG-63 cells grown on gold nanoparticle-modified PLA or unmodified PLA scaffolds for 3, 7, 14, or 21 days. Analyzed using two-way ANOVA. *$p < 0.05$ with respect to day 3 within each group; #$p < 0.05$ compared to the plated control: \$$p < 0.05$ compared to PLA. Data are $n = 5 \pm$ SD. (c) MTT cell viability assay was performed on human lung fibroblasts, HBE16, and Cos1 cells grown on gold nanoparticle-modified PLA or unmodified PLA scaffolds for 72 h. Analyzed using an unpaired t-test. *$p < 0.05$ compared to unmodified PLA scaffold control. (d) Cell viability assay performed using MTT on MG-63 cells grown on gold nanoparticle-modified 3D-printed PLA wafer for 24 h. Before cell seeding, wafers were incubated in human plasma for 24 hours. Analyzed using one-way ANOVA. *$p < 0.05$ compared to plated; #$p < 0.05$ compared to Au treated + Plasma. Data are $n = 6 \pm$ SD. (e) Protein adsorption was determined using a proteinase K digestion method. Gold-treated wafers were first treated with human plasma and subsequently left to incubate for 24 hours. Data are $n = 6 \pm$ SD. Analyzed by student t-test. *$P < 0.002$ compared to PLA.

cell models. These results indicate gold nanoparticles minimize cytotoxicity compared to un-modified PLA scaffolds.

Next, we incubated the gold nanoparticle-modified scaffolds in healthy human plasma or PBS for 48 hours. We then seeded MG-63 cells. Cells were grown for 3 days, and viability was measured using an MTT assay. The scaffolds that were incubated in plasma had significantly increased cell viability compared to scaffolds incubated in PBS (Fig. 7(d)). We then also attempted to quantify human plasma proteins that were bound to the surface of the scaffolds (Fig. 7(e)). The scaffolds were incubated in healthy human donor plasma for 48 h, washed, and then any proteins present were digested with proteinase K. Supernatants were collected and measured using a DC Lowry protein assay. Gold-nanoparticle-modified scaffolds had significantly higher levels of proteins present compared to un-modified PLA scaffolds (Fig. 7(e)).

The increased protein adsorption of the gold-treated and PLA wafers could be one of the major reasons behind the improved growth of MG63 cells on the gold nanoparticle modified wafers after incubation in human plasma. We also noted a significant increase in cell viability compared to the control. This finding corroborates the findings of Lebre *et al.* regarding the increased biocompatibility of gold nanoparticles coupled with albumin. These findings suggest that gold nanoparticles benefit from nonspecific binding with proteins that promote biocompatibility.[49]

These results show that the there is great potential in gold nanoparticle deposition on known biocompatible polymeric surfaces. We have demonstrated that cytotoxicity is mitigated in two main ways: (1) washing steps using sonication, pioneered in previous work,[29] (2) and the *in situ* synthesis and anchoring of the gold nanoparticles onto the polymeric surface. The preliminary biocompatibility data using the other cell lines (human Fibroblasts, Cos1, and HBE16) will be pursued in future work to better understand and compare the effects of various nanoparticle systems.

4. Conclusions

In conclusion, we report a reliable *in vitro* screening platform for nanoparticle-modified 3D printed scaffolds. We combine

two different plasma-assisted nanoparticle modification processes namely dusty plasma and plasma electroless reduction methods with a new 3D wafer design to assess this platform which can reliably study the materiobiology characteristics. The material characterization results especially SEM and laser confocal imaging have revealed that silica nanoparticle modification on the surface of the 3D scaffolds took place in a non-uniform manner. This is due to the mechanism of this plasma polymerization process which comprises 3 stages: nucleation, growth, and deposition. In our dusty plasma method, the nanoparticles form in the vapor phase and are then deposited onto the surface of the material which leads to the random and non-uniform coating. However, the plasma electroless reduction method was found to uniformly modify the surface of the 3D scaffolds with gold nanoparticles. TEM analysis demonstrated the uniformity of deposition and size of the gold nanoparticles (particle size being ~100 nm). The gold and silica nanoparticle-modified 96 and 24 well plate 3D wafer designs were used to study the biological response of these nanoparticle-modified scaffolds. The biological characterization suggests that the gold nanoparticle increases the viability of the cells and acts as cytoskeletal anchoring points for the osteosarcoma cells to grow. Also, the mineralization on the gold nanoparticle-modified scaffolds was significantly higher in comparison with control scaffolds. This suggests the improved bioactivity potential of gold nanoparticle-modified scaffolds. These results were very encouraging and could accelerate the development of gold nanoparticle-modified 3D scaffolds with better osteogenic potential. However, we do acknowledge the fact that the present study is not conclusive enough to fully establish the osteogenic potential of the gold nanoparticle-modified 3D scaffolds. In future studies, osteogenic potential could be elucidated further by gene expression arrays using RT-qPCR for osteo-related genes as well as utilization of undifferentiated blastocytes or stem cell studies wherein differentiation and other functions could be assessed after exposure to these nanoparticles. We believe that this study demonstrates great potential for multiple avenues of future exploration and serves as a proof of concept. In conclusion, this new design could operate as a screening platform that can be used to gather more reliable *in vitro* results on biocompatibility and bioactivity of nanoparticle-modified 3D printed scaffolds which can improve/enhance the *in vivo* success rate and thereby accelerate the translational potential of nanoparticle surface modified 3D printed scaffolds for tissue engineering applications.

Author contributions

Gerardo Hernández Moreno: conceptualization, methodology, verification, formal analysis, investigation, data curation, writing – original draft, visualization, and project administration. Vineeth M. Vijayan: conceptualization, validation, formal analysis, investigation, funding acquisition, data curation, writing – original draft, visualization, and project administration. Brian A. Halloran: resources, validation, investigation, and writing – review & editing. Namasivayam Ambalavanan: resources, validation, and writing – review & editing. Alexandria L. Hernández Nichols: validation, investigation, and writing & editing. John Bradford: validation and investigation. Renjith R. Pillai: validation and investigation. Vinoy Thomas: conceptualization, funding acquisition, resources, project administration, visualization, review & editing, and supervision.

Conflicts of interest

There are no conflicts of interest to declare. The manuscript has been approved by all authors listed in this publication.

Acknowledgements

The authors thank the following people and organizations for their contributions to the work: Mr Evan Eltinge, Keyence Corporation of America for the 3D Laser Scanning Confocal Microscope surface analysis; Ed Phillips for assistance in TEM imaging; VMV is thankful for the seed research grant funding from the UAH/NSF EPSCoR program. The authors are also thankful for the NSF EPSCoR program for the funding and support through the RII-Track-1 Cooperative Agreement OIA-2148653. Any statements, opinions, recommendations, or conclusions shared are those only of the authors and do not necessarily relay the official positions of the United States National Science Foundation (NSF).

References

1 G. Nikaeen, S. Abbaszadeh and S. Yousefinejad, *Nanomedicine*, 2020, **15**, 1501–1512.
2 X. Han, K. Xu, O. Taratula and K. Farsad, *Nanoscale*, 2019, **11**, 799–819.
3 R. S. Darweesh, N. M. Ayoub and S. Nazzal, *Int. J. Nanomed.*, 2019, **14**, 7643–7663.
4 M. Nasrollahzadeh, M. Sajjadi, G. J. Soufi, S. Iravani and R. S. Varma, *Nanomaterials*, 2020, **10**, 1072.
5 N. N. Zhang, X. F. Li, Y. Q. Deng, H. Zhao, Y. J. Huang, G. Yang, W. J. Huang, P. Gao, C. Zhou, R. R. Zhang, Y. Guo, S. H. Sun, H. Fan, S. L. Zu, Q. Chen, Q. He, T. S. Cao, X. Y. Huang, H. Y. Qiu and C. F. Qin, *Cell*, 2020, **182**, 1271–1283.
6 Y. Chen, M. Zhu, B. Huang, Y. Jiang and J. Su, *Biomater. Adv.*, 2022, **144**, 213232.
7 X. Han, A. Alu, H. Liu, Y. Shi, X. Wei, L. Cai and Y. Wei, *Bioact. Mater.*, 2022, **17**, 29–48.
8 Y. S. Chen, Y. C. Hung, I. Liau and G. S. Huang, *Nanoscale Res. Lett.*, 2009, **4**, 858–864.
9 J. Bahamonde, B. Brenseke, M. Y. Chan, R. D. Kent, P. J. Vikesland and M. R. Prater, *Toxicol. Pathol.*, 2018, **46**, 431–443.
10 S. B. Yaqoob, R. Adnan, R. M. Rameez Khan and M. Rashid, *Front. Chem.*, 2020, **8**, 376.
11 M. Umezawa, A. Onoda and K. Takeda, *Yakugaku Zasshi*, 2017, **137**, 73–78.
12 R. Wang, B. Song, J. Wu, Y. Zhang, A. Chen and L. Shao, *Int. J. Nanomed.*, 2018, **13**, 8487–8506.

13 H. Li, S. Pan, P. Xia, Y. Chang, C. Fu, W. Kong, Z. Yu, K. Wang, X. Yang and Z. Qi, *J. Biol. Eng.*, 2020, **14**, 14.
14 A. Cheng, A. Humayun, D. J. Cohen, B. D. Boyan and Z. Schwartz, *Biofabrication*, 2014, **6**, 045007.
15 A. H. Aghajanian, A. Bigham, A. Sanati, A. Kefayat, M. R. Salamat, M. Sattary and M. Rafienia, *Biomater. Adv.*, 2022, **137**, 212809.
16 A. Gupta and S. Singh, *Small*, 2022, e2201462.
17 Y. Kirmanidou, M. Sidira, A. Bakopoulou, A. Tsouknidas, O. Prymak, R. Papi, T. Choli-Papadopoulou, M. Epple, N. Michailidis, P. Koidis and K. Michalakis, *Dent. Mater.*, 2019, **35**, e220–e233.
18 D. Escorcia-Diaz, S. Garcia-Mora, L. Rendon-Castrillon, M. Ramirez-Carmona and C. Ocampo-Lopez, *Nanomaterials*, 2023, **13**, 2586.
19 L. Y. Koo, D. J. Irvine, A. M. Mayes, D. A. Lauffenburger and L. G. Griffith, *J. Cell Sci.*, 2002, **115**, 1423–1433.
20 J. Wolfram, M. Zhu, Y. Yang, J. Shen, E. Gentile, D. Paolino, M. Fresta, G. Nie, C. Chen, H. Shen, M. Ferrari and Y. Zhao, *Curr. Drug Targets*, 2015, **16**, 1671–1681.
21 B. Nikoobakht and M. A. El-Sayed, *Chem. Mater.*, 2003, **15**, 1957–1962.
22 R. Rudolf, B. Friedrich, S. Stopić, I. Anžel, S. Tomić and M. Čolić, *J. Biomater. Appl.*, 2012, **26**, 595–612.
23 R. Rudolf, P. Majerič, S. Tomić, M. Shariq, U. Ferčec, B. Budič, B. Friedrich, D. Vučević and M. Čolić, *J. Nanomater.*, 2017, **2017**, 9395012.
24 P. Xie, Y. Qi, R. Wang, J. Wu and X. Li, *Nanomaterials*, 2019, **9**, 1488.
25 G. Frens, *Nat. Phys. Sci.*, 1973, **241**, 20–22.
26 I. Hammami, N. M. Alabdallah, A. A. Jomaa and M. Kamoun, *J. King Saud Univ., Sci.*, 2021, **33**, 101560.
27 E. C. Cho, Q. Zhang and Y. Xia, *Nat. Nanotechnol.*, 2011, **6**, 385–391.
28 K. Chen, P. Ustriyana, F. Moore and N. Sahai, *ACS Biomater. Sci. Eng.*, 2019, **5**, 561–571.
29 V. M. Vijayan, M. Walker, R. R. Pillai, G. H. Moreno, Y. K. Vohra, J. J. Morris and V. Thomas, *ACS Appl. Mater. Interfaces*, 2022, **14**, 25065–25079.
30 V. M. Vijayan, B. S. Tucker, P. T. J. Hwang, P. S. Bobba, H. W. Jun, S. A. Catledge, Y. K. Vohra and V. Thomas, *J. Mater. Chem. B*, 2020, **8**, 2814–2825.
31 V. M. Vijayan, B. S. Tucker, P. S. Dimble, Y. K. Vohra and V. Thomas, *ACS Appl. Nano Mater.*, 2020, **3**, 7392–7396.
32 B. Molina-Martínez and L. M. Liz-Marzán, *Biomater. Biosyst.*, 2022, **6**, 100044.
33 L. Yang, S. Pijuan-Galito, H. S. Rho, A. S. Vasilevich, A. D. Eren, L. Ge, P. Habibovic, M. R. Alexander, J. de Boer, A. Carlier, P. van Rijn and Q. Zhou, *Chem. Rev.*, 2021, **121**, 4561–4677.
34 A. M. Cherian, J. Joseph, M. B. Nair, S. V. Nair, M. Vijayakumar and D. Menon, *Biomater. Adv.*, 2022, **142**, 213149.
35 S. P. Khan, G. G. Auner and G. M. Newaz, *Nanomedicine*, 2005, **1**, 125–129.
36 Z. Ma, Z. Mao and C. Gao, *Colloids Surf., B*, 2007, **60**, 137–157.
37 H. H. Hwang, S. You, X. Ma, L. Kwe, G. Victorine, N. Lawrence, X. Wan, H. Shen, W. Zhu and S. Chen, *Biofabrication*, 2021, **13**(2), 025007.
38 Z. Fang, J. Chen, Y. Zhu, G. Hu, H. Xin, K. Guo, Q. Li, L. Xie, L. Wang, X. Shi, Y. Wang and C. Mao, *Nat. Commun.*, 2021, **12**, 3757.
39 Y. Li, Y. Xiao and C. Liu, *Chem. Rev.*, 2017, **117**, 4376–4421.
40 Y. Raymond, C. Lehmann, E. Thorel, R. Benitez, A. Riveiro, J. Pou, M. C. Manzanares, J. Franch, C. Canal and M. P. Ginebra, *Biomater. Adv.*, 2022, **137**, 212807.
41 F. Afghah, M. Ullah, J. Seyyed Monfared Zanjani, P. Akkus Sut, O. Sen, M. Emanet, B. Saner Okan, M. Culha, Y. Menceloglu, M. Yildiz and B. Koc, *Biomed. Mater.*, 2020, **15**, 035015.
42 V. Fitzpatrick, Z. Martin-Moldes, A. Deck, R. Torres-Sanchez, A. Valat, D. Cairns, C. Li and D. L. Kaplan, *Biomaterials*, 2021, **276**, 120995.
43 X. Tang, Y. Qin, X. Xu, D. Guo, W. Ye, W. Wu and R. Li, *BioMed Res. Int.*, 2019, **2019**, 2076138.
44 C. Mandrycky, Z. Wang, K. Kim and D. H. Kim, *Biotechnol. Adv.*, 2016, **34**, 422–434.
45 V. M. Vijayan, G. Hernandez-Moreno and V. Thomas, in *Tissue Engineering*, ed. C. P. Sharma, T. Chandy, V. Thomas and F. G. Thankam, Academic Press, 2022, pp. 193–236.
46 M. T. Tavares, V. M. Gaspar, M. V. Monteiro, S. F. JP, C. Baleizao and J. F. Mano, *Biofabrication*, 2021, **13**(3), 035012.
47 C. Gandhimathi, Y. J. Quek, H. Ezhilarasu, S. Ramakrishna, B. H. Bay and D. K. Srinivasan, *Int. J. Mol. Sci.*, 2019, **20**(20), 5135.
48 S. W. Ha, M. Viggeswarapu, M. M. Habib and G. R. Beck, Jr., *Acta Biomater.*, 2018, **82**, 184–196.
49 K. Bolanos, M. J. Kogan and E. Araya, *Int. J. Nanomed.*, 2019, **14**, 6387–6406.
50 J. P. Bradford, B. Tucker, G. Hernandez-Moreno, P. Charles and V. Thomas, *J. Mater. Sci.*, 2021, **56**, 14717–14728.
51 F. Lebre, R. Sridharan, M. J. Sawkins, D. J. Kelly, F. J. O'Brien and E. C. Lavelle, *Sci. Rep.*, 2017, **7**, 2922.
52 Y. Pan, S. Neuss, A. Leifert, M. Fischler, F. Wen, U. Simon, G. Schmid, W. Brandau and W. Jahnen-Dechent, *Small*, 2007, **3**, 1941–1949.